



HCOOH distributions from IASI for 2008-2014: comparison with ground-based FTIR measurements and a global chemistry-transport model

5 M. Pommier^{1,*}, C. Clerbaux^{1,2}, P.-F. Coheur², E. Mahieu³, J.-F. Müller⁴, C. Paton-Walsh⁵, T. Stavrakou⁴, C. Vigouroux⁴

1 Sorbonne Universités, UPMC Univ. Paris 06; Université Versailles St-Quentin; CNRS/INSU, LATMOS-IPSL, Paris, France

10 2 Spectroscopie de l'Atmosphère, Chimie Quantique et Photophysique, Université Libre de Bruxelles (ULB), Brussels, Belgium

3 Institute of Astrophysics and Geophysics of the University of Liège, Liège, Belgium

4 Royal Belgian Institute for Space Aeronomy (BIRA-IASB), Avenue Circulaire 3, 1180 Brussels, Belgium

5 School of Chemistry, University of Wollongong, Wollongong, Australia

15 * Now at Norwegian Meteorological Institute, Oslo, Norway

Correspondence to: M. Pommier (matthieup@met.no)

Abstract.

Formic acid (HCOOH) is one of the most abundant volatile organic compounds in the atmosphere. It is a major contributor
20 to rain acidity in remote areas. There are however large uncertainties on its sources and sinks, and HCOOH is misrepresented by global chemistry-transport models. This work presents global distributions from 2008 to 2014 as derived from the measurements of the Infrared Atmospheric Sounding Interferometer (IASI), based on conversion factors between brightness temperature differences and representative retrieved total columns over seven regions: Africa N, Africa S, Amazonia, Atlantic, Australia, Pacific and Russia. The dependence of the thermal contrast is taking account in the
25 conversion method. This conversion presents errors lower than 20% for total columns ranging between 0.5 and 1×10^{16} molec/cm² but reaches higher values, up to 78%, for columns lower than 0.3×10^{16} molec/cm². Signatures from biomass burning events are highlighted, such as in the Southern Hemisphere and in Russia, as well as biogenic emission sources, e.g. over Eastern US. A comparison between 2008 and 2014 with ground-based FTIR measurements obtained at 4 locations (Maido and Saint-Denis at La Réunion, Jungfrauoch and Wollongong) is shown. Although IASI columns are found to
30 correlate well with FTIR data, a large bias (>100%) is found over the two sites at La Réunion. A better agreement is found at Wollongong with a negligible bias. The comparison also highlights the difficulty for IASI to retrieve the total columns over mountainous regions such as Jungfrauoch. A comparison of the retrieved columns with the global chemistry-transport model IMAGESv2 is also presented, showing the good representation of the seasonal and inter-annual cycles over America, Australia, Asia and Siberia. A global model underestimation of the distribution and a misrepresentation of the seasonal cycle
35 over India are also noted. A small positive trend in the IASI columns is also observed over Australia, Amazonia and India over 2008-2014 (from 0.7 to 1.5%/year), while a decrease of ~0.8%/year is measured over Siberia.



1. Introduction

40 Formic acid (HCOOH) is among one of the most abundant volatile organic compounds (VOCs) present in the atmosphere. Along with acetic acid it is a major contributor to the acidity of precipitation, especially in remote regions (Keene and Galloway, 1988; Andreae et al., 1988). HCOOH has small direct emissions by vegetation (Keene and Galloway, 1984, 1988), from ants (Graedel and Eisner, 1988), biomass burning (e.g. Goode et al., 2000), soils (Sanhueza and Andreae, 1991), agriculture (e.g., Ngwabie et al., 2008), and motor vehicles (Kawamura et al., 1985; Grosjean, 1989) but it is mainly a
45 secondary product from other organic precursors. The largest global chemical sources of HCOOH include isoprene, monoterpenes, other terminal alkenes (e.g., Neeb et al., 1997; Lee et al., 2006; Paulot et al., 2011), alkynes (Hatakeyama et al., 1986; Bohn et al., 1996), and acetaldehyde (Andrews et al., 2012; Clubb et al., 2012). HCOOH is mainly removed from the troposphere through wet and dry deposition, but also through oxidation by the OH radical to a lesser extent.

HCOOH is a short-lived species and its lifetime is mainly determined by the precipitation rate, ranging between 2 days
50 during the rainy season and 6 days in the dry season in the boundary layer (Sanhueza et al., 1996) and the global lifetime in the troposphere is 3–4 days (Paulot et al., 2011; Stavrou et al., 2012). Photochemical loss is relatively slow ($\tau \sim 25$ days), so that any HCOOH formed or vented outside of the boundary layer can be transported for long distances in the free troposphere (Paulot et al., 2011).

Our knowledge about sources and sinks of HCOOH is still incomplete despite numerous studies during this last decade. In
55 the current emissions inventories, as in the biogenic emission inventory MEGAN-MACC (Sindelarova et al., 2014), the main source regions are located in tropical regions as presented in Fig. 1 for the period between 2008 and 2010. A recent work shows a possible source of HCOOH over the Arctic Ocean (Jones et al., 2014). The study by Stavrou et al. (2012) highlights a misrepresentation of emission from tropical and boreal forest in models compared to total columns retrieved from Infrared Atmospheric Sounding Interferometer (IASI) observations by Razavi et al. (2011), and Millet et al. (2015),
60 Paulot et al. (2011) as well as Stavrou et al. (2012) point to the existence of one or more large missing sources. These studies suggest an important gap in our current understanding of hydrocarbon oxidation and/or the existence of an unknown direct flux of HCOOH.

Nadir looking atmospheric sensors allow to derive global distributions for trace gases, with a limited vertical sensitivity as compared to airborne or ground-based measurements. Their extended spatial coverage allows observing remote regions
65 which are sparsely studied by field campaigns. Only a few satellites provide tropospheric HCOOH observations, such as the nadir-viewing instrument IASI (e.g. Razavi et al., 2011) and the Tropospheric Emission Spectrometer (TES) (e.g. Cady-Pereira et al., 2014). The Michelson Interferometer for Passive Atmospheric Sounding (MIPAS) limb instrument provides monthly global distributions of HCOOH around 10 km (Grutter et al., 2010), and the solar-occultation Atmospheric Chemistry Experiment (ACE) (e.g. González Abad, 2009) in the upper troposphere.



70 The data used in this study are provided by IASI. This instrument has two important advantages: a low radiometric noise and
a high spatial coverage. HCOOH is a weak absorber, so that remains challenging to retrieve total column measurements from
the IASI radiance. Global distributions of HCOOH over land were initially derived using a method based on brightness
temperature difference and using forward simulations (Razavi et al., 2011). More recently, R'Honi et al. (2013) developed a
specific method to study extreme events occurring during the large fires in Russia in the summer 2010. These studies
75 however highlighted their discrepancies between the retrieved distributions and especially within enriched HCOOH air
masses as over large forest fires. In this paper, we present an update of the method, in order to derive HCOOH distributions
over both land and sea, suitable for both large and background concentrations over 2008-2014. Section 2 introduces the IASI
mission and explains the methodology used, based on an optimal estimation method (OEM) retrieval over selected areas,
used to design a fast retrieval methodology based on the brightness temperature difference and conversion factors. In Section
80 3, global distributions are shown; the products are compared to ground-based measurements and to the global chemistry-
transport model (CTM) IMAGESv2, providing an analysis of the seasonal and inter-annual variability of HCOOH columns.
The conclusions are given in Section 4.

2. IASI HCOOH columns

85 2.1. The IASI mission

IASI is a nadir-viewing Fourier Transform Spectrometer instrument. Currently two instruments are in orbit. The first model
was launched onboard the METOP-A platform in October 2006 providing now more than 8 years of observations. The
second instrument was launched in September 2012. Each instrument delivers near global coverage twice per day at around
9:30 local time (AM and PM) owing to the wide swath. IASI measures in the thermal infrared part of the spectrum, between
90 645 and 2760 cm^{-1} . It records radiance from the Earth's surface and the atmosphere with an apodized spectral resolution of
0.5 cm^{-1} , spectrally sampled at 0.25 cm^{-1} . IASI has a good radiometric performance, around 0.15 K (or around 2×10^{-6} W
 $\text{cm}^{-2} \text{sr}^{-1} / \text{cm}^{-1}$) in the HCOOH spectral range ($\sim 1105 \text{ cm}^{-1}$) for a reference blackbody at 280 K (Clerbaux et al., 2009).
As shown in Fig. 2, IASI is sensitive to the tropospheric HCOOH signal between 1 and 6 km. This plot shows the
normalized Jacobians over the spectral range used for the HCOOH retrieval (1095-1114 cm^{-1}), for a set of representative
95 geographical regions (see Fig 1. and details in the next section). These Jacobians represent the sensitivity of IASI and the
radiative transfer model to the abundance of HCOOH in a fixed atmosphere. This corresponds to the mean of the Jacobians
simulated from the selected spectra over the studied regions.

2.2 Retrieval approach

100 Processing 7 years (2008-2014) of IASI data using an iterative method such as the OEM (Rodgers, 2000) is computationally
demanding. Hence we have chosen a fast and robust approach based on brightness temperature differences (ΔBT) between



spectral channels with and without the signature of the target gas, to extract information without performing a full retrieval. In a second step, the ΔBT are converted into total columns of HCOOH using a set of data retrieved by OEM. This approach is adapted from the previous works for other IASI weak absorbers, such as methanol (Razavi et al. 2011), sulfur dioxide (Clarisse et al., 2008) and ammonia (Van Damme et al., 2014).

In the current work, the main difference with the previous IASI HCOOH determination in Razavi et al. (2011) is the use of retrieved total columns over selected regions to determine conversion factors, instead of the use of forward simulations. In Razavi et al. (2011), the reason invoked for performing only forward simulations for HCOOH was the unstable character of the retrievals. With the retrieval settings chosen here, we rely on the retrieved columns since 82% of the selected spectra were successfully retrieved (Tab. 1) and the mean Root Mean Square (RMS) difference between the observed and fitted spectra is about $2.5 \times 10^{-6} \text{ W cm}^{-2} \text{ sr}^{-1} / \text{cm}^{-1}$. This is close to the IASI estimated radiometric noise.

The conversion factors allowing the conversion of ΔBT to total columns are determined by using the parameters from a linear regression, obtained by correlating ΔBT with HCOOH total columns retrieved with an OEM implemented in the line-by-line radiative transfer model. The spectroscopic parameters are from the HITRAN 2008 database (Rothman et al., 2009), using the set of HCOOH spectroscopic line parameters of Vander Auwera et al. (2007). The retrievals have been done with the same a priori profile as in Razavi et al. (2011) but with a very large variability (350%). This variability was chosen based on the retrieval settings used by Razavi et al. (2011). The reference channels used for the calculation of ΔBT were chosen on both sides of the HCOOH channel (1105 cm^{-1}), i.e. at 1103.0 and 1109.0 cm^{-1} .

In the OEM-based retrieval, only cloud free scenes (when the cloud coverage for the pixel is below 2%) have been used. The total columns of interfering species in the studied spectral range, such as ozone, ammonia and CFC-12, in addition to the partial columns of water vapor, were simultaneously retrieved. The details of the retrieval parameters are given in Table 2. The EUMETSAT L2 operational data were used, and day-time and night-time data with a positive thermal contrast (TC) are taken into account. The TC is defined as the temperature difference between the surface and the air just above. Negative TC data were excluded, as these were found to deteriorate the correlation ΔBT -total column.

The OEM-based retrieval has been performed over 7 geographical regions shown as blue boxes in Fig. 1. These include 5 source areas (in Southern Africa, Northern Africa, Amazonia, Australia, Russia) and 2 remote areas (over the Atlantic and Pacific Oceans). These 7 regions are representative of different conditions: emission sources, remote area, areas influenced by long-range transport, over land and over sea. We have retrieved the five first days of each month in 2009 over the 7 regions, allowing the characterization of the seasonal variation. The localization of each area and the number of retrieved spectra are given in Table 1.

From these retrievals, we derive a linear regression between the retrieved total columns and the ΔBT , illustrated by Fig. 3 (left panel). A good correlation is found ($r = 0.74$) between both parameters. The density of the distribution is also given (Fig. 3, right panel), showing a larger density of data between 0.3 and 0.6 K on the ΔBT axis, and between 0.4 and 0.6×10^{16}



molec/cm² for the total column. As in Razavi et al. (2011), this relationship is found to depend on the local TC conditions.

135 This dependence is characterized by the color code showing the TC values on Fig. 3 (left panel). For example, a ΔBT equal to 0.5 K generally corresponds to a total column close to 0 at high TC, or around 2×10^{16} molec/cm² at very low TC.

2.3 Development of updated IASI HCOOH dataset

2.3.1 Reduction of the thermal contrast dependence

140 To account for the TC dependence in the ΔBT -total column relationship as shown in Fig. 3 (left panel), we have performed forward simulations with different thermal contrasts, using the observation made in the regions and periods listed in Table 1. We artificially modified the surface temperature for each atmospheric profile by ± 5 K. In total, three TC conditions were simulated: TC_{ref} , $TC_{ref}+5K$, $TC_{ref}-5K$. These simulations were performed with the a priori as initial total column. In total, 13155 spectra were simulated. The linear regression between TC and ΔBT is illustrated in Fig 4a. A fair correlation is found,
 145 with r equal to 0.6. Based on this linear regression, a corrected ΔBT (ΔBT_{TC}) is defined using equation (1):

$$\Delta BT_{TC} = \Delta BT - (TC \times a_1 + a_2) \quad (1)$$

with $a_1 = 0.0138$ and $a_2 = 0.3502$. These ΔBT_{TC} still present a high correlation with the OEM-based total columns ($r = 0.75$) and the TC dependence disappears, as shown in Fig 4b. We then deduce a relationship between the total column and the measured ΔBT as below:

$$x = b_1 \times \Delta BT_{TC} + b_2 \quad (2)$$

150 with x being the total column in 10^{16} molec/cm², $b_1 = 1.5713$ and $b_2 = 0.6792$.

Note that this conversion can lead to negative total columns. If we eliminate all the negative values and keep only all the positive values, we would introduce an artificial bias in the average. For comparisons, only negative averages were filtered out.

155 2.3.2 Error estimation

This technique has a low computational cost but the drawback of the method is the difficulty to characterize the retrieval in terms of vertical sensitivity (averaging kernels not available) and the error budget.

The total error of the ΔBT approach can be described by three terms: 1) the instrumental error, 2) the error caused by the conversion from ΔBT to total column, 3) the error originating in the OEM retrievals. Simulations were performed for the
 160 data set over the 7 regions, using 6 initial total columns, i.e. by perturbing the a priori (-50%, the reference a priori, +50%, +100%, +200%, +350%). In total, 26310 forward simulations were used. In the simulations, the temperature profile used is from EUMETSAT operational level 2.



A Gaussian distributed random noise (with $\sigma = 0.15$ K, corresponding to the noise in the studied spectral range) was added to the BT channels used for the ΔBT calculation from the simulated spectra. Then the conversion formula (Eq. 2) was applied to the calculated ΔBT .

Figure 5 shows the histogram of the relative difference (RD) between the calculated total columns and the true total columns used as input in the forward simulations. The RD is defined as the difference between the calculated total columns and the true total columns, divided by the latter. Positive RDs imply that the calculated total column is higher than the true column. This histogram presents a mean of $\sim 1.6\%$ and a standard deviation around 69% . Note that these results agree with those from Razavi et al. (2011), finding a mean RD equal to -0.8% and a standard deviation of 60% . The relative difference is not impacted by the TC or the H_2O profile but it depends on the HCOOH total column. Fig. 6 shows the dependence of the mean RD to the HCOOH total column a priori used as input to the forward simulation. Large positive RDs (up to 78%) are found for low total columns whereas negative RDs prevail for large HCOOH columns (lower than 35%). In other words, the retrieval based on brightness temperature differences tends to overestimate the low value of the true columns, and underestimate the high values.

3. Analysis of the dataset

3.1 Global Distributions

Mean HCOOH global distributions (averaged on a $0.5^\circ \times 0.5^\circ$ grid) from IASI for the 2008-2014 period are presented in Fig. 7 and compared with columns obtained using the retrieval method of Razavi et al. (2011). Note that Razavi et al. (2011) retrieved only total columns over land. Except over Indonesia, lower values are observed over the source regions with the updated dataset. The previous section shows that large positive RDs are expected for very low true columns. Even if the columns from Razavi et al. (2011) are not the true columns, this could explain why the total columns for this study are higher over remote areas (e.g. deserts) than those obtained using the methodology described by Razavi et al. (2011).

Yearly global distributions between 2008 and 2014 with the updated dataset are also presented in Fig. 8 (on a $1^\circ \times 1^\circ$ grid). These distributions highlight well the recurring source regions detected by IASI such as over Equatorial Africa, the North of Australia, Amazonia and India, and also the long-range transport such as over the Atlantic Ocean from Africa. The long-range transport over the ocean (Atlantic, Indian and Pacific) was not investigated in Razavi et al. (2011). The retrieved columns over the Atlantic Ocean are consistent with the FTIR data from ship cruises reported in the study of Paulot et al. (2011). They showed a gradient of columns from the Poles to the Equator, with higher values between $0-10^\circ N$, up to 3.5×10^{16} molec/cm² with a large variability, the monthly mean being lower than 0.5×10^{16} molec/cm².

Several hotspots and distributions are detected and are numbered from (1) to (10) in Fig. 8.

(1) Among the years, specific patterns are distinguished, in particular a large hotspot over Russia (close to Moscow) in 2010 as documented by R'Honi et al. (2013), due to intense forest fires during the summer and also in 2012 over Siberia (Fig. 8).



195 The current dataset presents a mean total column twice lower (2.0×10^{16} molec/cm²) than the mean derived using the conversion from Razavi et al. (2011) (4.2×10^{16} molec/cm²), within the emission area (50°-55°N, 30°-70°E), on 27 July - 27 August 2010, in agreement with the conclusions from R'Honi et al. (2013).

(2) Large columns were also found over Sakha Republic and over Khabarovsk Krai (Russia) in 2008 and 2012.

(3) The North American boreal emissions were larger between 2008 and 2010 than the other years, around the Hudson Bay.

200 (4) We also note lower columns over Louisiana and Texas in 2008 and in 2014 compared to the other years.

(5) Larger total columns were measured over Northern Australia between 2012 and 2014, in comparison to the period from 2008 to 2010.

The monthly means over the 7 years are also presented with an animation (Fig. S1) in the Supplement. It highlights the seasonal variation of the HCOOH distribution around the world. The animation reveals clear variations in the HCOOH
205 distribution due to the seasonality of biomass burning and vegetation growth. For example, large total columns were observed during September and October 2008, 2012, 2014 in the Southern Hemisphere (over Amazonia, Africa and Australia). In 2010, the same features were also noted except for Australia.

In June 2010 and 2012, there were also large concentrations over Eastern Russia, close to Khabarovsk Krai, compared to the other years in this region (see label (2)). Even though intense fires were detected in June 2012 in this region, it was not the
210 case in June 2010 (see maps on <http://lance-modis.eosdis.nasa.gov/cgi-bin/imagery/firemaps.cgi>). The absence of forest fire and the lack of hotspots in the biogenic emission inventory (Fig. 1) in this region points to the presence of an unidentified source, possibly of biogenic origin.

(6) Large columns were similarly retrieved over a large region encompassing Laos, Thailand and Myanmar in April 2010, 2012, 2013 and 2014. It matches well with the locations of fires hotspots detected by MODIS.

215 (7) In August 2010, larger total columns were retrieved along the Euphrates River compared to the other years.

(8) These monthly distributions also highlight hotspots over the US, besides those shown in the annual distributions. In summer 2011, large signatures over the US were not only confined close to the coast but high total columns were also detected in the Mid-Western US such as over Kansas, Mississippi, Missouri or Oklahoma. These states are assigned as a biogenic emission region of VOCs by Millet et al. (2015), acting as secondary source of HCOOH. In July 2012, the
220 emissions over the US were mostly confined to the Eastern part.

(9) The Asian HCOOH outflow is well captured over the western Pacific. The total columns broadly agree with the measurements from the aircraft PEM-West-B campaign conducted in February-March 1994 (Talbot et al., 1997a; 1997b) over a large region covering the latitudes 0°-60°N and the longitudes 110°-180°E. Indeed, measured HCOOH mixing ratios profiles during the campaign mostly ranged around 100-150 pptv from the boundary layer to about 12 km altitude, with peak
225 values of up to 4 ppbv in fresh (< 2 days) plumes originating in China. Using these profiles, we estimate that this corresponds approximately to columns ranging from 0.2 to 0.9×10^{16} molec/cm². Over the remote Pacific, the IASI total



columns are larger than measured during the aircraft PEM-Tropics-A campaign in August–December 1996 (e.g. Talbot et al., 1999). They measured mixing ratios of the order of 20–40 ppbv in the boundary layer and 50–100 pptv in the free troposphere, corresponding to estimated total columns of $0.1\text{--}0.2 \times 10^{16}$ molec/cm². This overestimation is in agreement with
230 the error budget from Fig. 6.

(10) Over India, the largest total columns are observed from March to June.

3.2 Comparison with ground-based FTIR measurements

The IASI HCOOH retrieved columns in this work have been compared with ground-based FTIR measurements. This
235 comparison was done without smoothing the data since the averaging kernels (AKs) were not provided by our retrieval method. This comparison is presented at four sites: Jungfraujoch (46.55°N 7.98°E) in Switzerland, Wollongong in Australia (34.41°S 150.88°E), Saint-Denis (20.88°S 55.45°E) and Maito (21.07°S 55.39°E) at La Réunion Island (Fig. 9). The current retrieved columns have also been evaluated with those using the methodology from Razavi et al (2011) over the same sites (Fig. 10).

240 The current retrieved columns were also compared with a set of columns retrieved by OEM around the sites. For each OEM-based retrieved column, the corresponding column using the conversion factors was calculated showing the current dataset and the OEM-based retrieval are in agreement way (correlation ranging from 0.7 to 0.8, with an underestimation of the columns calculated with the conversion factors between 6 and 15%). It is also worth to note that similar biases were found between these columns retrieved by OEM around the ground-based locations and the FTIR columns than between the
245 columns retrieved in this work and the FTIR ones.

Averaging kernels were also unavailable for the FTIR measurements performed at Jungfraujoch (extended from Zander et al., 2010) and at Wollongong (Paton-Walsh et al., 2005). The measurements at Saint-Denis and Maito reach a maximum sensitivity between about 3 and 12 km as described in Vigouroux et al. (2012) and shown in Fig. 2. These AKs and the Jacobians presented in Fig. 2 show that FTIR and IASI are both mostly sensitive to the free troposphere but that the FTIR
250 measurements present a broader vertical sensitivity, reaching higher altitudes than IASI.

A difficulty in comparisons of satellite columns with ground-based measurements over mountain sites like Jungfraujoch over the Swiss Alps (3.6 km altitude) or Maito at La Réunion (2.2 km altitude), is the difference of altitude between the FTIR sites and the co-located IASI ground pixel height. To account for the altitude dependence, both the IASI and the FTIR total columns are normalized to the sea level altitude using:

$$C_{\text{corrected}} = C \times \exp(H/7.4) \quad (3)$$

255

where H represents the ground measurement height (in km) and C is the total column (in 10^{16} molec/cm²). This normalization relies on the assumption that the HCOOH mixing ratio is constant as a function of altitude. Although crude, this procedure improves the comparisons.



The time series of the IASI and FTIR columns over the selected sites are shown in Fig. 9. The comparison used IASI data
260 collocated within 0.5° of the site location in both latitude and longitude. To keep a sufficient amount of IASI data to
compare, daily averages were used. A more stringent criterion of ± 2 h was tested but provided similar results, except over
Maido where the correlation increased to 0.6 without improvement of the bias. Over all sites, the broad patterns of seasonal
and inter-annual variations are similarly captured by IASI and the ground-based FTIR.

The comparison between the ground-based measurements and the total column derived from the IASI spectra may be
265 affected by sampling differences associated e.g. to cloudiness. IASI may be able to measure through clear skies in the
vicinity of the station when the FTIR data are not available due to localized cloud. Moreover, despite the use of strict of
stricter co-location criteria (spatial and temporal), most mismatches in peak values still could be a result of mismatches in the
spatial and temporal scales of the measurements being compared.

The correlation coefficients and the biases between FTIR and IASI are also provided for each year in Table 3. Over
270 Jungfrauoch (Fig. 9), large total columns are measured by the ground-based instrument during the spring and the summer
for each year. These large values are not captured by IASI data, causing a large bias of 1.14×10^{16} molec/cm² on average. The
comparison at Jungfrauoch presents the lowest correlation coefficient among the four stations. This might be caused to some
extent by the error associated to the normalization to the sea level, largest at the high-altitude of Jungfrauoch.

The seasonal cycle obtained from IASI agrees well with FTIR data over both sites at La Réunion (correlation coefficient $r =$
275 0.77 at St-Denis, up to 0.85 in 2011; see Table 3) but the columns from the IASI retrieval show a large positive bias at both
sites ($>100\%$). The overestimation by IASI is especially large for background columns, i.e. between February and July, when
FTIR columns are of the order of 0.15×10^{16} molec/cm². This increase of the bias for lower values of the true column is
qualitatively consistent with the dependence of the error associated to the conversion from brightness temperatures on the
magnitude of the true column (Fig. 6): the expected error is lower than 20% for columns ranging between 0.5 and 1×10^{16}
280 molec/cm², and close to 80% for columns lower than 0.3×10^{16} molec/cm². In addition, the difference in the altitude range of
the vertical sensitivity between IASI and the FTIR could also contribute to the biases at Saint-Denis and Maido. Regarding
the time series at La Réunion, it is worth noting the large columns measured in October 2010 and 2011 over Saint-Denis,
which correspond to enriched plumes from Africa, are seen in the spatial distributions (Fig. S1).

At Wollongong, IASI and ground-based FTIR background levels are in broad agreement. The correlation is highest in 2008.
285 The peaks in the HCOOH columns in October 2012, 2013 and in Nov 2014 observed by both instruments are also seen in the
distributions in Fig. S1. As in the case of La Reunion data, a larger positive bias is found when the FTIR total columns are
low ($<0.5 \times 10^{16}$ molec/cm²).

The FTIR measurements are also used to evaluate the current HCOOH columns with those using the conversion from Razavi
et al. (2011) (Fig. 10). The colocation criteria have been enlarged to $\pm 4^\circ$ since the evaluation shown in Stavrakou et al.
290 (2012) with the data of Razavi et al. (2011) around the sites, used only averaged columns on a $0.5^\circ \times 0.5^\circ$ grid. Fig. 10 shows



the distribution of the relative differences with the FTIR measurements for both methodologies. It provides information about the bias, the normalized bias and the correlation coefficient. At all sites, the distribution is more spread out with the conversion from Razavi et al. (2011). The correlation coefficient is largely improved with the updated dataset, except over Saint-Denis where it is similar. The bias is also significantly reduced with the updated dataset except over Jungfraujoch. This difference over Jungfraujoch is coherent with the previous comparison (Fig. 9) since the updated dataset is underestimated compared to the FTIR measurements.

295

Overall, the current dataset presents higher correlation and lower bias than the columns from Razavi et al. (2011).

3.3 Comparison with IMAGESv2

The IMAGESv2 global CTM runs at 2° resolution in latitude and 2.5° resolution in longitude. The model is resolved at 40 vertical levels, from the surface up to the pressure of 44 hPa (Stavrakou et al., 2011). The biogenic emissions of isoprene (believed to be the most important precursor of HCOOH) are obtained from MEGAN-MOHYCAN (Stavrakou et al. 2014). The vegetation fire emissions are from GFEDv3 (van der Werf et al., 2010). This dataset distinguishes emissions from savanna, woodland, and forest fires, agricultural waste burning, peatlands, deforestation and degradation fires. The anthropogenic emissions are constructed from a mix of inventories: REASv2 in Asia (Kurokawa et al. 2013), NEI in USA (from www.epa.gov/ttnchie1/trends/), EMEP (obtained from www.ceip.at/webdab-emission-database/emissions-as-used-in-emp-models/) in Europe, and RETRO database (Schultz et al., 2007) for the rest of world.

305

3.3.1 Seasonal variation

For the sake of comparison, the IASI HCOOH total columns have been averaged to the horizontal model grid resolution. The IASI and the model total columns have also been averaged by season, defined as: December-January-February (DJF), March-April-May (MAM), June-July-August (JJA) and September-October-November (SON) over the 7 years, between 2008 and 2014. Figure 11 presents these global distributions for IASI and the model. For each season, we find that the IASI total columns are higher than those from IMAGESv2 simulations. This highlights the difficulty to predict the measured concentrations by models as found in previous modelling studies such as Stavrakou et al. (2012) and Paulot et al. (2011).

315

During the winter (DJF), the model shows large total columns over Equatorial Africa and Asia while IASI only detects large values over Africa.

In spring (MAM), the CTM largely underestimates the distributions over Africa compared to IASI.

320

In summer (JJA), the emissions from fires seem to be the primary cause for strong HCOOH enhancements in the CTM (Africa, Amazonia, boreal regions: Canada and Eastern Siberia) although biogenic emissions (Southeastern US) and anthropogenic activities (Eastern China) also produce visible enhancements. In the IASI distributions, enhancements associated to fires are less prominent over North and South America. IASI reveals larger total columns over Africa in JJA



than over South America while the CTM shows roughly the same values over both regions. Compared with the CTM, IASI
also shows larger HCOOH columns over midwestern US, India and semiarid regions in Southwestern Russia and
325 Kazakhstan.

During fall (SON), the columns from IASI over the southern hemispheric biomass burning emission regions (South America,
Africa and Australia) are larger than over Asia (India and China) and over Indonesia while those simulated by the model are
quite similar for these regions.

330 3.3.2 Inter-annual variation

The global and seasonal distributions from IASI suggest an underestimation of the modelled columns and a
misrepresentation of some emission sources. Figure 12 presents the time-series over the areas identified by black boxes in
Fig. 1. These regions are: AMER (North America), AMAZ (Amazonia), AFRI (Africa), SIBE (Central Siberia), INDI
(India), ASIA (Asia) and AUST (Australia).

335 Over all regions, these time series confirm a large bias of IASI in comparison to the simulations. The seasonal variation is
however well represented, except over India, where the seasonal cycle is out of phase. This phase difference is coherent with
the cycle shown on the global distribution (Fig. 11). The calculated linear trend is also provided, based on the annual IASI
mean (blue dots in Fig. 12). Over three regions (North America, Africa and Asia), the trend is negligible (0.2-0.4%/year) but
a small increase is noted over Australia, Amazonia and India ($1.5\pm 0.5\%$ /year, $0.9\pm 0.7\%$ /year and $0.7\pm 0.1\%$ /year
340 respectively). A decrease of $0.8\pm 0.9\%$ /year is also observed over Siberia.

Over Amazonia, the large peak in 2010 due to large forest fires emissions (e.g. Hooghiemstra et al. 2012) is well represented
in the model and captured by IASI; however, the peak in the IASI data occurs one month later than in the CTM. A similar
shift was already observed between the CO and NH₃ observations from IASI (Withburn et al., 2015). This HCOOH shift
could be partly due to the difference of altitude in the HCOOH vertical distributions. IASI detects the plumes in the free
345 troposphere, whereas the IMAGES columns reflect more directly the surface emissions. The mean altitude of the maximum
in the HCOOH vertical profile from the model is located around 2.8 km for this region and close to 2 km in August 2010,
while the maximum of vertical sensitivity from IASI is located at higher altitude. This assumes that transport time is close to
one month which is longer than the known mean transport time between the boundary layer and the upper troposphere. Over
Siberia, the summer 2010 and at a lesser extent the summer 2012, were exceptional in terms of large HCOOH emissions, as
350 noted with the global distributions shown in Fig. 8. As revealed by the correlation coefficients, the seasonal cycle is very
well captured over Asia ($r=0.75$), Australia ($r=0.92$), Siberia ($r=0.94$) and North America ($r=0.94$).

The double peaks (~March and September) over Africa are explained by the shift of emission seasons on either side of the
Equator. Over Africa, the correlation is lower, due to two factors: there is a shift of one month between IASI and the CTM in
the maximum of columns, and the higher columns from IASI remain longer in time than those simulated (especially between



355 the peak around January with the CTM and the one around February-March for IASI). A difference of altitude in the
detection of HCOOH between the CTM and IASI could not explain IASI detected higher total columns during more than
one month in the troposphere in March. Around March-April, the mean altitude of maximum in the simulated columns is
around 4 km, close to the altitude of maximum vertical sensitivity from IASI, showing that the CTM and IASI should detect
the same enriched HCOOH plume.

360

4. Conclusions

Global distributions of HCOOH are derived from IASI radiance spectra, using conversion factors between representative
retrieved total columns and selected radiance channels (ΔBT). This paper presents seven years of HCOOH measurements
recorded by IASI. A limitation of this dataset is its lack of characterization for vertical sensitivity due to the conversions
365 technique used, even though the maximum sensitivity is shown to be in the mid-troposphere. This approach has the
significant advantage of reducing the computing time necessary to analyze the large amount of data and to provide a global
representation of the HCOOH distribution around the world, including ocean and land scenes, and emission sources as well
as remote areas.

IASI provides global distributions of HCOOH, highlighting the long-range transport of tropospheric HCOOH over the
370 Atlantic Ocean and the detection of source regions, e.g. biomass burning areas over Amazonia, Africa, Australia and Siberia.
Other source regions are detected such as the Mid-eastern United States in 2011 or over India.

The comparison with an atmospheric model and to a lesser extent with ground based FTIR observations remains challenging.
Despite large biases in many cases, we show that the inter-annual and the seasonal variations are well captured by IASI
when compared with ground-based FTIR measurements and the IMAGESv2 CTM. The best overall correlation with the
375 FTIR is obtained at Saint-Denis over La Réunion ($r=0.77$) but both sites at La Réunion present the larger bias ($>100\%$ lower
than IASI). High correlations are obtained with the CTM, in particularly over America, Australia, Siberia and Asia, with
correlation coefficients ranging from 0.75 to 0.94. This comparison also points out a misrepresentation of the distribution
between IASI and the CTM over India and Africa and a global underestimation of the distribution by the CTM. A small
decreasing trend during the 7-yr period is also observed over Siberia, while a small increase is noted over India, Amazonia
380 and Australia (0.7%/year, 0.9%/year and 1.5%/year respectively).

The HCOOH columns from IASI will require further evaluation and probably improvements to narrow down the biases but
the dataset available spans now 7 years and it will likely contribute to a better understanding of the tropospheric HCOOH
budget. The dataset will be made available through the Ether database (<http://ether.ipsl.jussieu.fr>) for further scientific
studies. This 7-year record will be completed by the data provided by IASI/MetOp-B, launched at the end of 2012, and
385 IASI/MetOp-C to be launched in 2018. The IASI program will be followed up (after 2022) by the IASI-NG mission aboard
the MetOp-SG satellite series (Clerbaux and Crevoisier, 2013; Crevoisier et al., 2014). This new instrument will be



characterized by improved spectral resolution and lower radiometric noise. It will lead to a better vertical resolution, along with improved accuracy and detection threshold.

390

Acknowledgments. IASI was developed and built under the responsibility of Centre National des Etudes Spatiales (CNES) and flies onboard the MetOp satellite as part of the EUMETSAT Polar system. The authors acknowledge the Ether French atmospheric database (<http://ether.ipsl.jussieu.fr>) for providing the IASI LIC data and access to emission inventories via ECCAD (<http://ether.ipsl.jussieu.fr/eccad>). The French scientists are grateful to CNES for financial support. We also
395 gratefully acknowledge Yasmina R'Honi and Lieven Clarisse (ULB) for their help with the HCOOH retrieval. The authors would like to thank the other researchers involved in the ground-based solar remote sensing program at Wollongong (including Nicholas B. Jones, David Griffith, Nicholas Deutscher and Voltaire Velazco) and the Australian Research Council for its support for the NDACC site at Wollongong, most recently as part of project DP110101948. Acknowledgements are addressed to the Université de La Réunion and CNRS (LACy-UMR8105 and UMS3365) for their support of the OPAR
400 station (Observatoire de Physique de l'Atmosphère de la Réunion). The authors gratefully acknowledge C. Hermans, F. Scolas, and B. Langerock from BIRA-IASB, and J.-M. Metzger from Université de La Réunion, for the Reunion Island measurements. The University of Liège contribution to the present work has been supported by the F.R.S. – FNRS, the Belgian Science Policy Office (BELSPO), Brussels, the Fédération Wallonie-Bruxelles and MeteoSwiss (GAW-CH program). We thank the International Foundation High Altitude Research Stations Jungfraujoch and Gornergrat (HFSJG,
405 Bern). We are grateful to all Belgian colleagues who contributed to the acquisition of the FTIR data at Jungfraujoch. The Reunion Island measurements have mainly been supported by the A3C project (PRODEX Program of BELSPO). The research was supported by BELSPO and ESA through the IASI.Flow project (Prodex arrangement 4000111403).

410

415



References

- 420 Andreae, M. O., Andreae, T. W., Talbot, R. W., and Harriss, R. C.: Formic and acetic acid over the central Amazon region, Brazil. I. Dry season, *J. Geophys. Res.*, 93, 1616–1624, doi:10.1029/JD093iD02p01616, 1988.
- Andrews, D. U., Heazlewood, B. R., Maccarone, A. T., Conroy, T., Payne, R. J., Jordan, M. J. T., and Kable, S. H.: Photo-tautomerization of acetaldehyde to vinyl alcohol: a potential route to tropospheric acids, *Science*, 337, 1203–1206, 2012.
- 425 Bohn, B., Siese, M., and Zetzsch, C.: Kinetics of the OH+C₂H₂ reaction in the presence of O₂, *J. Chem. Soc. Faraday T.*, 92, 1459–1466, 1996.
- 430 Cady-Pereira, K. E., Chaliyakunnel, S., Shephard, M. W., Millet, D. B., Luo, M., and Wells, K. C.: HCOOH measurements from space: TES retrieval algorithm and observed global distribution, *Atmos. Meas. Tech.*, 7, 2297–2311, doi:10.5194/amt-7-2297-2014, 2014.
- Clarisse, L., Coheur, P. F., Prata, A. J., Hurtmans, D., Razavi, A., Phulpin, T., Hadji-Lazaro, J., and Clerbaux, C.: Tracking and quantifying volcanic SO₂ with IASI, the September 2007 eruption at Jebel at Tair, *Atmos. Chem. Phys.*, 8, 7723–7734, doi:10.5194/acp-8-7723-2008, 2008.
- 435 Clerbaux, C., Boynard, A., Clarisse, L., George, M., Hadji-Lazaro, J., Herbin, H., Hurtmans, D., Pommier, M., Razavi, A., Turquety, S., Wespes, C., and Coheur, P.-F.: Monitoring of atmospheric composition using the thermal infrared IASI/MetOp sounder, *Atmos. Chem. Phys.*, 9, 6041–6054, doi:10.5194/acp-9-6041-2009, 2009.
- 440 Clerbaux C., C., and Crevoisier, C.: New Directions: Infrared remote sensing of the troposphere from satellite: Less, but better, *Atmospheric Environment*, 72, 24–26, doi:10.1016/j.atmosenv.2013.01.057, 2013.
- 445 Clubb, A. E., Jordan, M. J. T., Kable, S. H., and Osborn, D. L.: Phototautomerization of Acetaldehyde to vinyl alcohol: a primary process in UV-irradiated acetaldehyde from 295 to 335nm, *J. Phys. Chem. Lett.*, 3, 3522–3526, 2012.
- Coheur, P. F., Clerbaux, C., and Colin, R.: Spectroscopic measurements of halocarbons and hydrohalocarbons by satellite-borne remote sensors, *J. Geophys. Res.*, 108, NO. D4, 4130, doi:10.1029/2002JD002649, 2003.
- 450 Crevoisier, C., Clerbaux, C., Guidard, V., Phulpin, T., Armante, R., Barret, B., Camy-Peyret, C., Chaboureaud, J.-P., Coheur, P.-F., Crépeau, L., Dufour, G., Labonnote, L., Lavanant, L., Hadji-Lazaro, J., Herbin, H., Jacquinet-Husson, N., Payan, S., Péquignot, E., Pierangelo, C., Sellitto, P., and Stubenrauch, C.: Towards IASI-New Generation (IASI-NG): impact of improved spectral resolution and radiometric noise on the retrieval of thermodynamic, chemistry and climate variables, *Atmos. Meas. Tech.*, 7, 4367–4385, doi:10.5194/amt-7-4367-2014, 2014.
- 455 González Abad, G., Bernath, P. F., Boone, C. D., McLeod, S. D., Manney, G. L., and Toon, G. C.: Global distribution of upper tropospheric formic acid from the ACE-FTS, *Atmos. Chem. Phys.*, 9, 8039–8047, doi:10.5194/acp-9-8039-2009, 2009.
- 460 Goode, J., Yokelson, R., Ward, D., Susott, R., Babbitt, R., Davies, M., and Hao, W.: Measurements of excess O₃, CO₂, CO, CH₄, C₂H₄, C₂H₂, HCN, NO, NH₃, HCOOH, CH₃COOH, HCHO, and CH₃OH in 1997 Alaskan biomass burning plumes by airborne Fourier transform infrared spectroscopy (AFTIR), *J. Geophys. Res.*, 105, 22147, doi:10.1029/2000JD900287, 2000.
- Graedel, T. and Eisner, T.: Atmospheric formic acid from formicine ants: a preliminary assessment, *Tellus B*, 40, 335–339, 1988.
- 465 Grosjean, D.: Organic acids in southern California air: ambient concentrations, mobile source emissions, in situ formation and removal processes, *Environ. Sci. Technol.*, 23, 1506–1514, 1989.
- 470 Grutter, M., Glatthor, N., Stiller, G. P., Fischer, H., Grabowski, U., Höpfner, M., Kellmann, S., Linden, A., and von Clarmann, T.: Global distribution and variability of formic acid as observed by MIPAS-ENVISAT, *J. Geophys. Res.*, 115, D10303, doi:10.1029/2009JD012980, 2010.
- Hatakeyama, S., Washida, N., and Akimoto, H.: Rate constants and mechanisms for the reaction of hydroxyl (OH) radicals with acetylene, propyne, and 2-butyne in air at 297±2K, *J. Phys. Chem.*, 6, 90, 173–178, 1986.
- 475 Hooghiemstra, P. B., Krol, M. C., van Leeuwen, T. T., van der Werf, G. R., Novelli, P. C., Deeter, M. N., Aben, I., and Röckmann, T.: Interannual variability of carbon monoxide emission estimates over South America from 2006 to 2010, *J. Geophys. Res.*, 117, D15308, doi:10.1029/2012JD017758, 2012.
- 480 Jones, B. T., Muller, J. B. A., O'Shea, S. J., Bacak, A., Le Breton, M., Bannan, T. J., Leather, K. E., Murray Booth, A., Illingworth, S., Bower, K., Gallagher, M.W., Allen, G., Dudley Shallcross, E., Bauguitte, S. J.-B., Pyle, J. A., Percival, C. J.:



- Airborne measurements of HC(O)OH in the European Arctic: A winter summer comparison, *Atmospheric Environment*, 99, Pages 556–567, doi:10.1016/j.atmosenv.2014.10.030, 2014.
- 485 Kawamura, K., Ng, L., and Kaplan, I.: Determination of organic acids (C1-C10) in the atmosphere, motor exhausts, and engine oils, *Environ. Sci. Technol.*, 19, 1082–1086, 1985.
- Keene, W. and Galloway, J.: Organic acidity in precipitation of North America, *Atmos. Environ.*, 18, 2491–2497, 1984.
- 490 Keene, W. C. and Galloway, J. N.: The biogeochemical cycling of formic and acetic acids through the troposphere: An overview of current understanding, *Tellus B*, 40, 322–334, 1988.
- Kurokawa, J., Ohara, T., Morikawa, T., Hanayama, S., Janssens-Maenhout, G., Fukui, T., Kawashima, K., and Akimoto, H.: Emissions of air pollutants and greenhouse gases over Asian regions during 2000–2008: Regional Emission inventory in ASia (REAS) version 2, *Atmos. Chem. Phys.*, 13, 11019–11058, doi:10.5194/acp-13-11019-2013, 2013.
- 495 Lee, A., Goldstein, A. H., Kroll, J. H., Ng, N. L., Varutbangkul, V., Flagan, R. C., and Seinfeld, J. H.: Gas-phase products and secondary aerosol yields from the photooxidation of 16 different terpenes, *J. Geophys. Res.*, 111, D17305, doi:10.1029/2006JD007050, 2006.
- 500 Millet, D. B., Baasandorj, M., Farmer, D. K., Thornton, J. A., Baumann, K., Brophy, P., Chaliyakunnel, S., de Gouw, J. A., Graus, M., Hu, L., Koss, A., Lee, B. H., Lopez-Hilfiker, F. D., Neuman, J. A., Paulot, F., Peischl, J., Pollack, I. B., Ryerson, T. B., Warneke, C., Williams, B. J., and Xu, J.: A large and ubiquitous source of atmospheric formic acid, *Atmos. Chem. Phys. Discuss.*, 15, 4537–4599, doi:10.5194/acpd-15-4537-2015, 2015.
- 505 Neeb, P., Sauer, F., Horie, O., and Moortgat, G. K.: Formation of hydroxymethyl hydroperoxide and formic acid in alkene ozonolysis in the presence of water vapour, *Atmos. Environ.*, 31, 1417–1423, 1997.
- Ngwabie, N. M., Schade, G. W., Custer, T. G., Linke, S., and Hinz, T.: Abundances and flux estimates of volatile organic compounds from a dairy cowshed in Germany, *J. Environ. Qual.*, 37, 565–573, 2008.
- Paton-Walsh, C., Jones, N. B., Wilson, S. R., Haverd, V., Meier, A., Griffith, D. W. T., and Rinsland, C. P.: Measurements of trace gas emissions from Australian forest fires and correlations with coincident measurements of aerosol optical depth, *Journal of Geophysical Research-Atmospheres*, 110(D24), 2005.
- 515 Paulot, F., Wunch, D., Crounse, J. D., Toon, G. C., Millet, D. B., DeCarlo, P. F., Vigouroux, C., Deutscher, N. M., González Abad, G., Notholt, J., Warneke, T., Hannigan, J. W., Warneke, C., de Gouw, J. A., Dunlea, E. J., De Mazière, M., Griffith, D. W. T., Bernath, P., Jimenez, J. L., and Wennberg, P. O.: Importance of secondary sources in the atmospheric budgets of formic and acetic acids, *Atmos. Chem. Phys.*, 11, 1989–2013, doi:10.5194/acp-11-1989-2011, 2011.
- 520 Razavi, A., Karagulian, F., Clarisse, L., Hurtmans, D., Coheur, P. F., Clerbaux, C., Müller, J. F., and Stavrakou, T.: Global distributions of methanol and formic acid retrieved for the first time from the IASI/MetOp thermal infrared sounder, *Atmos. Chem. Phys.*, 11, 857–872, doi:10.5194/acp-11-857-2011, 2011.
- 525 R'Honi, Y., Clarisse, L., Clerbaux, C., Hurtmans, D., Dufлот, V., Turquety, S., Ngadi, Y., and Coheur, P.-F.: Exceptional emissions of NH₃ and HCOOH in the 2010 Russian wildfires, *Atmos. Chem. Phys.*, 13, 4171–4181, doi:10.5194/acp-13-4171-2013, 2013.
- 530 Rodgers, C. D.: Inverse methods for atmospheric sounding: theory and practice, Ser. Atmos. Ocean. Planet. Phys. 2, World Sci., Hackensack, NJ, 2000.
- Rothman, L. S., Gordon, I. E., Barbe, A., Benner, D. C., Bernath, P. F., Birk, M., Boudon, V., Brown, L. R., Campargue, A., Champion, J., Chance, K., Coudert, L. H., Dana, V., Devi, V. M., Fally, S., Flaud, J., Gamache, R. R., Goldman, A., Jacquemart, D., Kleiner, I., Lacombe, N., Lafferty, W. J., Mandin, J., Massie, S. T., Mikhailenko, S. N., Miller, C. E., Moazzen-Ahmadi, N., Naumenko, O. V., Nikitin, A. V., Orphal, J., Perevalov, V. I., Perrin, A., Predoi-Cross, A., Rinsland, C. P., Rotger, M., Simeckova, M., Smith, M. A. H., Sung, K., Tashkun, S. A., Tennyson, J., Toth, R. A., Vandaele, A. C., and Vander Auwera, J.: The HITRAN 2008 molecular spectroscopic database, *J. Quant. Spectrosc. Radiat. Transfer*, 110, 533–572, doi:10.1016/j.jqsrt.2009.02.013, 2009.
- 535 Sanhueza, E. and Andreae, M.: Emission of formic and acetic acids from tropical savanna soils, *Geophys. Res. Lett.*, 18, 1707–1710, 1991.
- 540 Sanhueza, E., Figueroa, L., and Santana, M.: Atmospheric formic and acetic acids in Venezuela, *Atmos. Environ.*, 30, 1861–1873, 1996.
- 545



- 550 Schultz, M. G., Backman, L., Balkanski, Y., Bjoerndalsaeter, S., Brand, R., Burrows, J. P., Dalsoeren, S., de Vasconcelos, M., Grodtmann, B., Hauglustaine, D. A., Heil, A., Hoelzemann, J. J., Isaksen, I. S. A., Kaurola, J., Knorr, W., Ladstaetter-Weissenmayer, A., Mota, B., Oom, D., Pacyna, J., Panasiuk, D., Pereira, J. M. C., Pulles, T., Pyle, J., Rast, S., Richter, A., Savage, N., Schnadt, C., Schulz, M., Spessa, A., Staehelin, J., Sundet, J. K., Szopa, S., Thonicke, K., van het Bolscher, M., van Noije, T., van Velthoven, P., Vik, A. F., and Wittrock, F.: REanalysis of the TROpospheric chemical composition over the past 40 years (RETRO): A long-term global modeling study of tropospheric chemistry, Jülich/Hamburg, Germany, 48/2007 report on Earth System Science of the Max Planck Institute for Meteorology, Hamburg, <http://retro.enes.org>, ISSN 1614-1199, 2007.
- 555 Sindelarova, K., Granier, C., Bouarar, I., Guenther, A., Tilmes, S., Stavrakou, T., Müller, J.-F., Kuhn, U., Stefani, P., and Knorr, W.: Global data set of biogenic VOC emissions calculated by the MEGAN model over the last 30 years, *Atmos. Chem. Phys.*, 14, 9317-9341, doi:10.5194/acp-14-9317-2014, 2014.
- 560 Stavrakou, T., Guenther, A., Razavi, A., Clarisse, L., Clerbaux, C., Coheur, P.-F., Hurtmans, D., Karagulian, F., De Mazière, M., Vigouroux, C., Amelynck, C., Schoon, N., Laffineur, Q., Heinesch, B., Aubinet, M., Rinsland, C., and Müller, J.-F.: First space-based derivation of the global atmospheric methanol emission fluxes, *Atmos. Chem. Phys.*, 11, 4873-4898, doi:10.5194/acp-11-4873-2011, 2011.
- 565 Stavrakou, T., Müller, J.-F., Peeters, J., Razavi, A., Clarisse, L., Clerbaux, C., Coheur, P.-F., Hurtmans, D., De Mazière, M.: Satellite evidence for a large source of formic acid from boreal and tropical forests, *Nature Geoscience*, 5, 26-30, doi:10.1038/ngeo1354(2012), 2012.
- 570 Stavrakou, T., Müller, J.-F., Bauwens, M., De Smedt, I., Van Roozendael, M., Guenther, A., Wild, M., and Xia, X.: Isoprene emissions over Asia 1979–2012: impact of climate and land-use changes, *Atmos. Chem. Phys.*, 14, 4587-4605, doi:10.5194/acp-14-4587-2014, 2014.
- 575 Talbot, R. W., Dibb, J. E., Lefer, B. L., Scheuer, E. M., Bradshaw, J. D., Sandholm, S. T., Smyth, S., Blake, D. R., Blake, N. J., Sachse, G. W., Collins, J. E., Gregory, G. L.: Large-scale distributions of tropospheric nitric, formic, and acetic acids over the western Pacific basin during wintertime, *J. Geophys. Res.*, 102(D23), 28303–28313, doi:10.1029/96JD02975, 1997a.
- 580 Talbot, R. W., Dibb, J. E., Lefer, B. L., Bradshaw, J. D., Sandholm, S. T., Blake, D. R., Blake, N. J., Sachse, G. W., Collins, J. E., Heikes, B. G., Merrill, J. T., Gregory, G. L., Anderson, B. E., Singh, H. B., Thornton, D. C., Bandy, A. R., and Poeschel, R. F.: Chemical characteristics of continental outflow from Asia to the troposphere over the western Pacific Ocean during February-March 1994: Results from PEM-West B, *J. Geophys. Res.*, 102(D23), 28255–28274, doi:10.1029/96JD02340, 1997b.
- 585 Talbot, R. W., Dibb, J. E., Scheuer, E. M., Blake, D. R., Blake, N. J., Gregory, G. L., Sachse, G. W., Bradshaw, J. D., Sandholm, S. T., and Singh, H. B.: Influence of biomass combustion emissions on the distribution of acidic trace gases over the Southern Pacific basin during austral springtime, *J. Geophys. Res.*, 104(D5), 5623-5634, 1999.
- 590 Van Damme, M., Clarisse, L., Heald, C. L., Hurtmans, D., Ngadi, Y., Clerbaux, C., Dolman, A. J., Erisman, J. W., and Coheur, P. F.: Global distributions, time series and error characterization of atmospheric ammonia (NH₃) from IASI satellite observations, *Atmos. Chem. Phys.*, 14, 2905-2922, doi:10.5194/acp-14-2905-2014, 2014.
- 595 Vander Auwera, J., Didriche, K., Perrin, A., and Keller, F.: Absolute line intensities for formic acid and dissociation constant of the dimer, *The J. Chem. Phys.*, 126, 124311, doi:10.1063/1.2712439, 2007.
- 595 van der Werf, G. R., Randerson, J. T., Giglio, L., Collatz, G. J., Mu, M., Kasibhatla, P. S., Morton, D. C., DeFries, R. S., Jin, Y., and van Leeuwen, T. T.: Global fire emissions and the contribution of deforestation, savanna, forest, agricultural, and peat fires (1997–2009), *Atmos. Chem. Phys.*, 10, 11707–11735, doi:10.5194/acp-10-11707-2010, 2010.
- 600 Vigouroux, C., Stavrakou, T., Whaley, C., Dils, B., Dufлот, V., Hermans, C., Kumps, N., Metzger, J.-M., Scolas, F., Vanhaelewyn, G., Müller, J.-F., Jones, D. B. A., Li, Q., and De Mazière, M.: FTIR time-series of biomass burning products (HCN, C₂H₆, C₂H₂, CH₃OH, and HCOOH) at Reunion Island (21° S, 55° E) and comparisons with model data, *Atmos. Chem. Phys.*, 12, 10367-10385, doi:10.5194/acp-12-10367-2012, 2012.
- 605 Whitburn, S., Van Damme, M., Kaiser, J.W., van der Werf, G.R., Turquety, S., Hurtmans, D., Clarisse, L., Clerbaux, C., Coheur, P.-F.: Ammonia emissions in tropical biomass burning regions: Comparison between satellite-derived emissions and bottom-up fire inventories. *Atmos. Env.*, 121, 42-54, doi:10.1016/j.atmosenv.2015.03.015, 2015.
- Zander, R., Duchatelet, P., Mahieu, E., Demoulin, P., Roland, G., Servais, C., Auwera, J. V., Perrin, A., Rinsland, C. P., and Crutzen, P. J.: Formic acid above the Jungfrauoch during 1985–2007: observed variability, seasonality, but no long-term background evolution, *Atmos. Chem. Phys.*, 10, 10047-10065, doi:10.5194/acp-10-10047-2010, 2010.



610 **Table 1** Selected regions used for the retrieval. The localization of each area and the number of spectra retrieved during the studied period are provided. The numbers correspond to the total number of successfully retrieved spectra and those given in parentheses to the total number of spectra in each region.

Region	Localization	Number of retrieved spectra
Africa N	6-7°N 18-22°E	265 (358)
Africa S	12-14°S 20-24°E	788 (1083)
Amazonia	6-10°S 43-45°W	682 (739)
Atlantic	22-24°N 42-45°W	675 (737)
Australia	14-15°S 131-133°E	218 (271)
Pacific	20-22°S 140-142°E	472 (492)
Russia	50-54°N 60-62°E	538 (781)

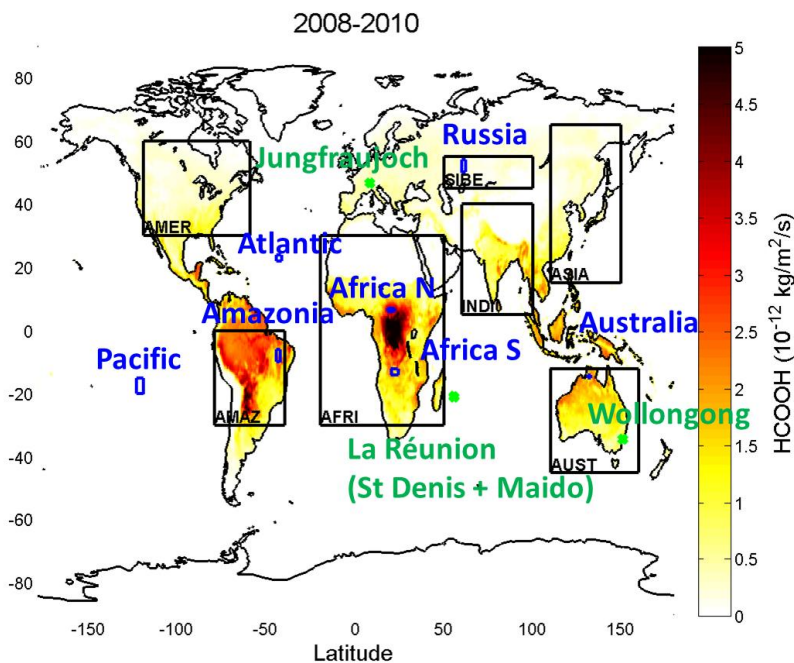
Table 2 Retrieval parameters used in this work.

Parameters	Layers	A priori	Variability
H ₂ O	0-10 km: five 2 km thick layers 10-20 km: two 5 km thick layers	EUMETSAT operational level 2	20%
O ₃	total column	standard atmosphere	20%
NH ₃	ditto	standard atmosphere	20%
HCOOH	ditto	Razavi et al. (2011)	350%
CFC-12	ditto	Coheur et al. (2003)	20%

615

Table 3 Correlation coefficient (in *italic*), mean bias in 10¹⁶ molec/cm², normalized mean bias (square brackets) in percent, between the daily FTIR measurements and the IASI co-located data. The IASI data are chosen at ±0.5° around the site location. The number of coincidence days is given in parentheses.

FTIR station	2008	2009	2010	2011	2012	2013	2014
Jungfraujoch	<i>0.33</i> -1.10 [-71.8] (57)	<i>0.06</i> -1.21 [-72.9] (53)	<i>0.23</i> -1.26 [-73.7] (69)	<i>0.49</i> -0.99 [-69.0](91)	<i>0.47</i> -1.15 [-72.4] (97)	<i>0.54</i> -1.24 [-71.4] (106)	<i>0.43</i> - 71.1] (78)
Wollongong	<i>0.77</i> -0.07 [-11.2] (50)	<i>0.16</i> 0.01 [2.9] (79)	<i>0.56</i> 0.03 [6.1] (44)	<i>0.60</i> -0.02 [-3.5] (96)	<i>0.63</i> -0.01 [-1.1] (124)	<i>0.69</i> -0.03 [-5.1] (106)	<i>0.57</i> 0 [0.6] (56)
Saint-Denis (La Réunion)	-	<i>0.69</i> 0.28 [110.1] (82)	<i>0.75</i> 0.24 [100.1] (72)	<i>0.85</i> 0.27 [100.6] (97)	-	-	-
Maïdo (La Réunion)	-	-	-	-	-	<i>0.35</i> 0.28 [131.2] (60)	<i>0.53</i> 0.28 [117.7] (49)



620 **Figure 1.** MEGAN-MACC HCOOH emissions for the period between 2008 and 2010 on a $0.5^\circ \times 0.5^\circ$ grid. The green stars
correspond to the location of the FTIR measurements, the 7 selected regions used for the retrievals and described in Table 1
are highlighted in blue, and the black boxes are the regions used for the comparison with IMAGESv2.

625

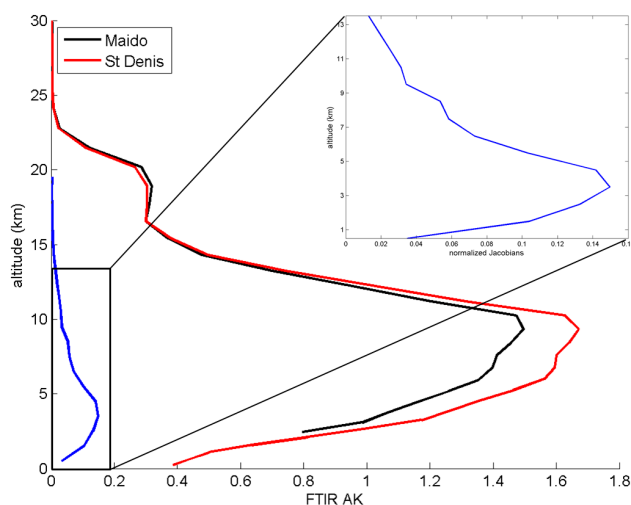


Figure 2. Mean normalized Jacobians of all retrieved spectra (over the 7 selected regions) as a function of altitude (blue),
superimposed to mean total column AK for the FTIR ground-based measurements over Maido (black) and Saint-Denis (red)
at La Réunion. Both stations are shown by green stars in Fig 1. Both FTIR stations have a degree of freedom of signal (DFS)
close to 1.

630

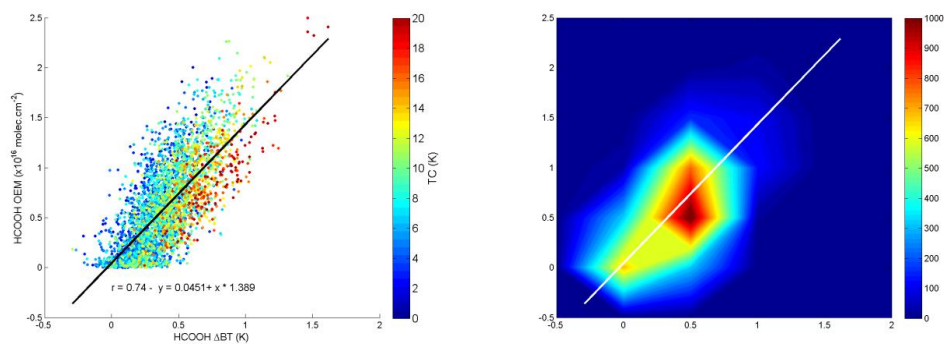


Figure 3. Left: Scatter plot between all the retrieved total columns using the Optimal Estimation Method (OEM) and the corresponding HCOOH Δ BT. The black line corresponds to the linear regression. Each data is colored based on its thermal contrast value. Right: Distribution of points density from the scatter plot. The number of points is highlighted with the color scale. The linear regression is also reported by a white line.

635

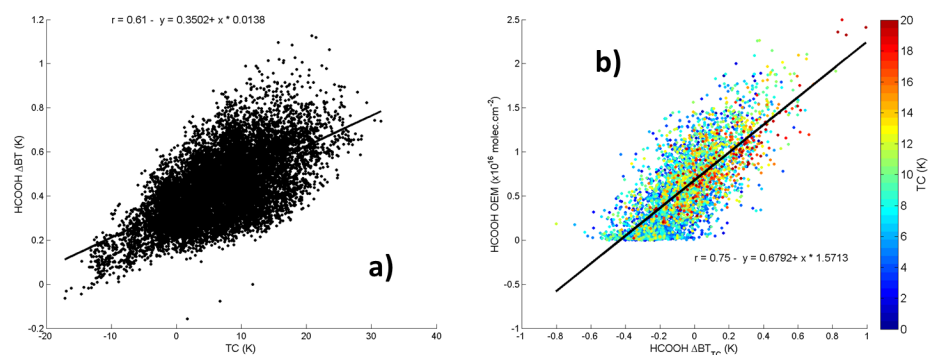
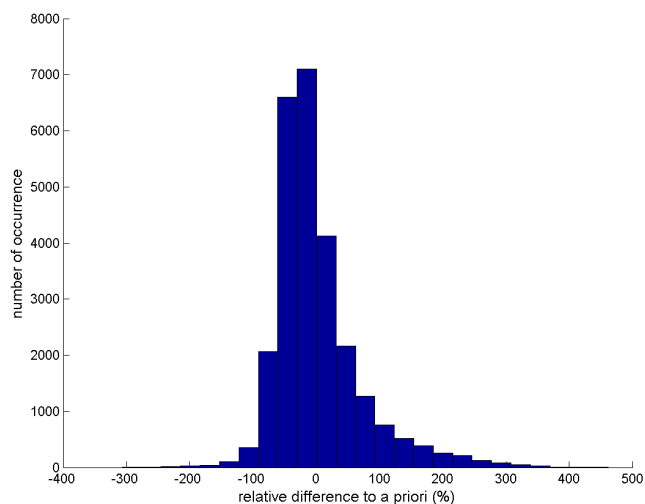
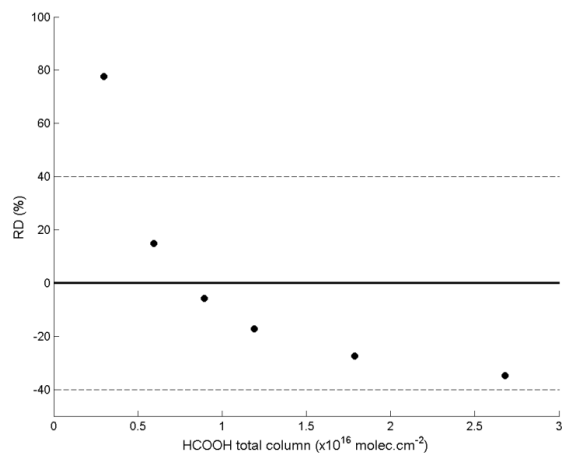


Figure 4. a: Scatter plot between the simulated Δ BT and the TC for one fixed HCOOH total column (0.6×10^{16} molec/cm 2). b: Scatter plot between the HCOOH retrieved total columns using the Optimal Estimation Method (OEM) and the corrected HCOOH Δ BT $_{TC}$. Δ BT $_{TC}$ corresponds to the HCOOH Δ BT taking account the TC dependence, given by the equation in the panel (a). Each data is colored based on its thermal contrast value as in Fig. 3 (left panel).

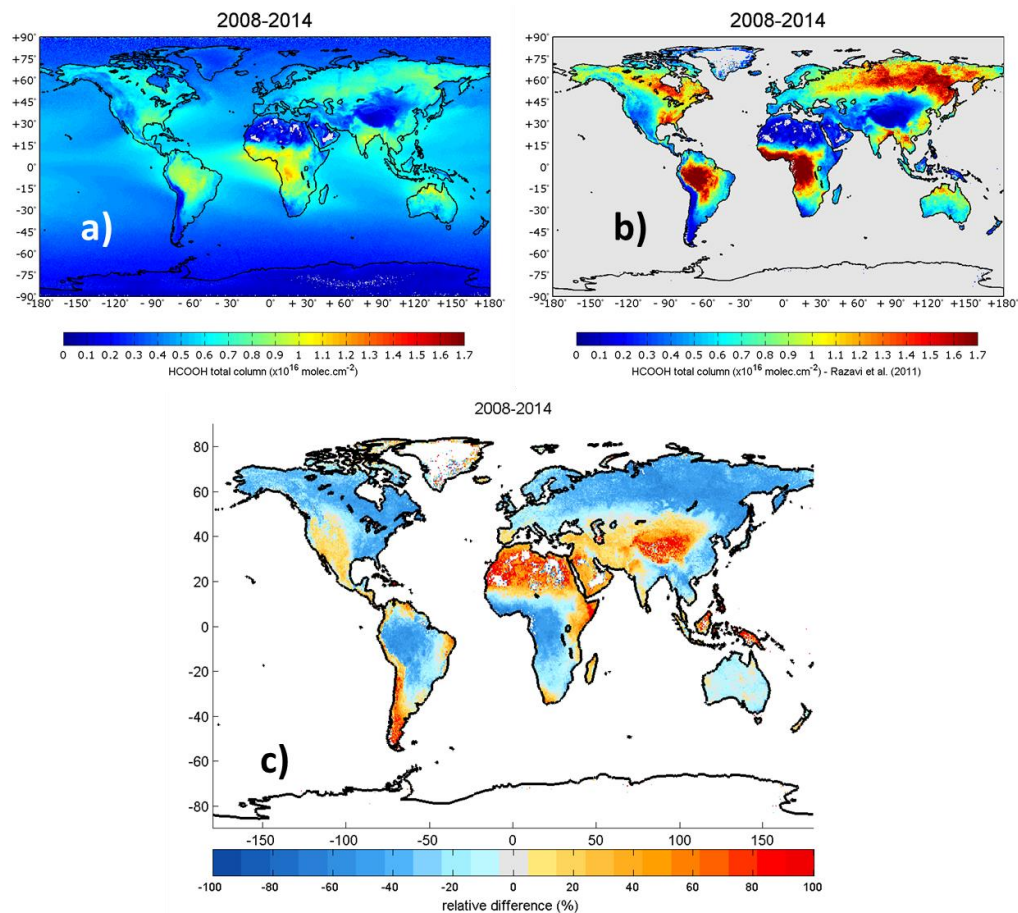
640



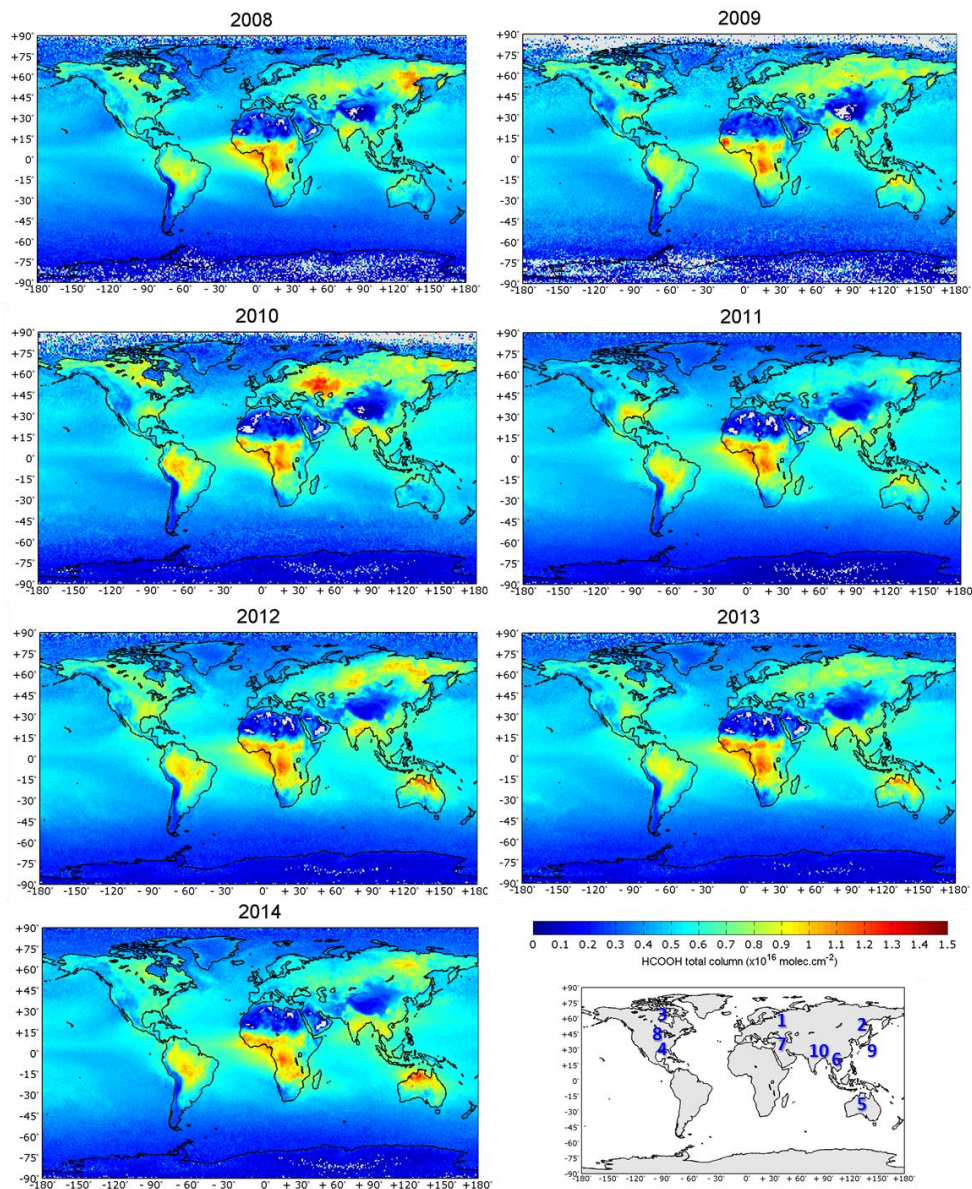
645 **Figure 5.** Histogram of the relative differences between the calculated total columns (derived from the ΔBT conversion) and the a priori total columns (used as input in the forward simulations). The a priori total columns are defined as the reference.



650 **Figure 6.** Variation of the mean relative difference between the total columns derived from the ΔBT conversion and the a priori total columns (used as input in the forward simulations) according to the a priori used. The black solid line corresponds to a relative difference equal to 0 and the dashed black lines to $\pm 40\%$.



655 **Figure 7.** Mean HCOOH global distribution between 2008 and 2014, derived using the IASI radiance observations on a $0.5^\circ \times 0.5^\circ$ grid with the retrieval from this work (a), using the methodology described by Razavi et al. (2011) (b) and the relative difference between both distributions in percent (c). The relative difference is defined as: $(\text{HCOOH}_{\text{this work}} - \text{HCOOH}_{\text{Razavi et al. (2011)}}) / \text{HCOOH}_{\text{Razavi et al. (2011)}}$.



660

Figure 8. Annual HCOOH global distribution from 2008 to 2014, derived using the IASI radiance observations on a $1^\circ \times 1^\circ$ grid. Different sources or distributions described in the text are numbered in blue on the bottom-right map.

665

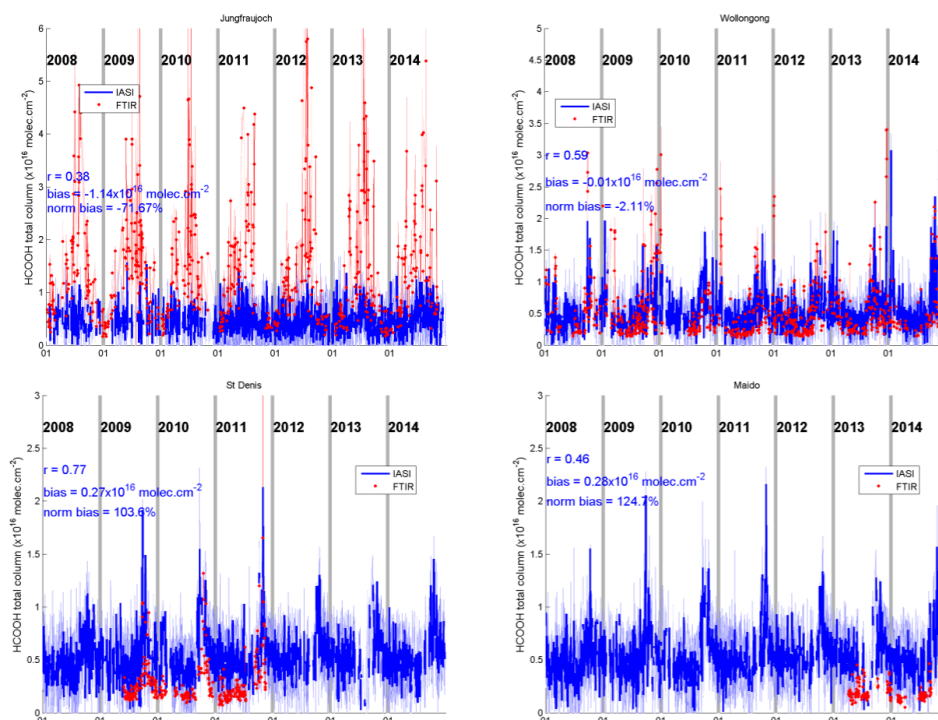


Figure 9. Time series of HCOOH daily means over Jungfraujoch (top-left), Wollongong (top-right), Saint-Denis (bottom-left) and Maïdo (bottom-right) between 2008 and 2014 for IASI (blue) and the ground-based FTIR (red) measurements. The IASI data are collocated at $\pm 0.5^\circ$ around the site location. The correlation coefficient, the mean bias and the normalized mean bias for all years is given in blue on each plot. The blue shade error bar corresponds to the standard deviation on the IASI daily means. The altitude of the stations is: 3.6 km for Jungfraujoch, 20 m for Wollongong, 50 m for Saint-Denis, 2.2 km for Maïdo.

670

675

680

685

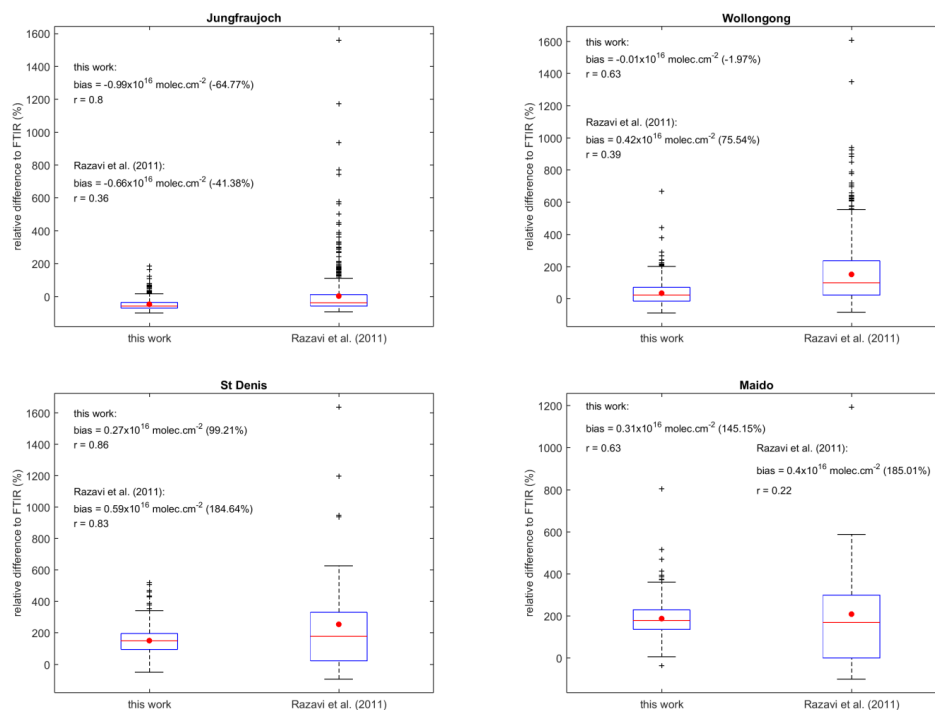


Figure 10. Box and whisker plots showing mean (red central circle), median (red central line), 25th and 75th percentile (blue box edges) of the relative difference between the HCOOH derived using the IASI radiance observations from this work or using the conversion from Razavi et al. (2011) and the FTIR measurements for each station: Jungfraujoch, Wollongong, Saint-Denis and Maido. The whiskers encompass values from 25th-1.5×(75th-25th) to the 75th+1.5×(75th-25th). This range covers more than 99 % of a normally distributed dataset. The outliers are represented individually by black crosses. For this comparison, the IASI data are collocated at ±4° around the site location. The mean bias, the normalized mean bias (in parentheses) and the correlation coefficient are given for both methods.

690

695

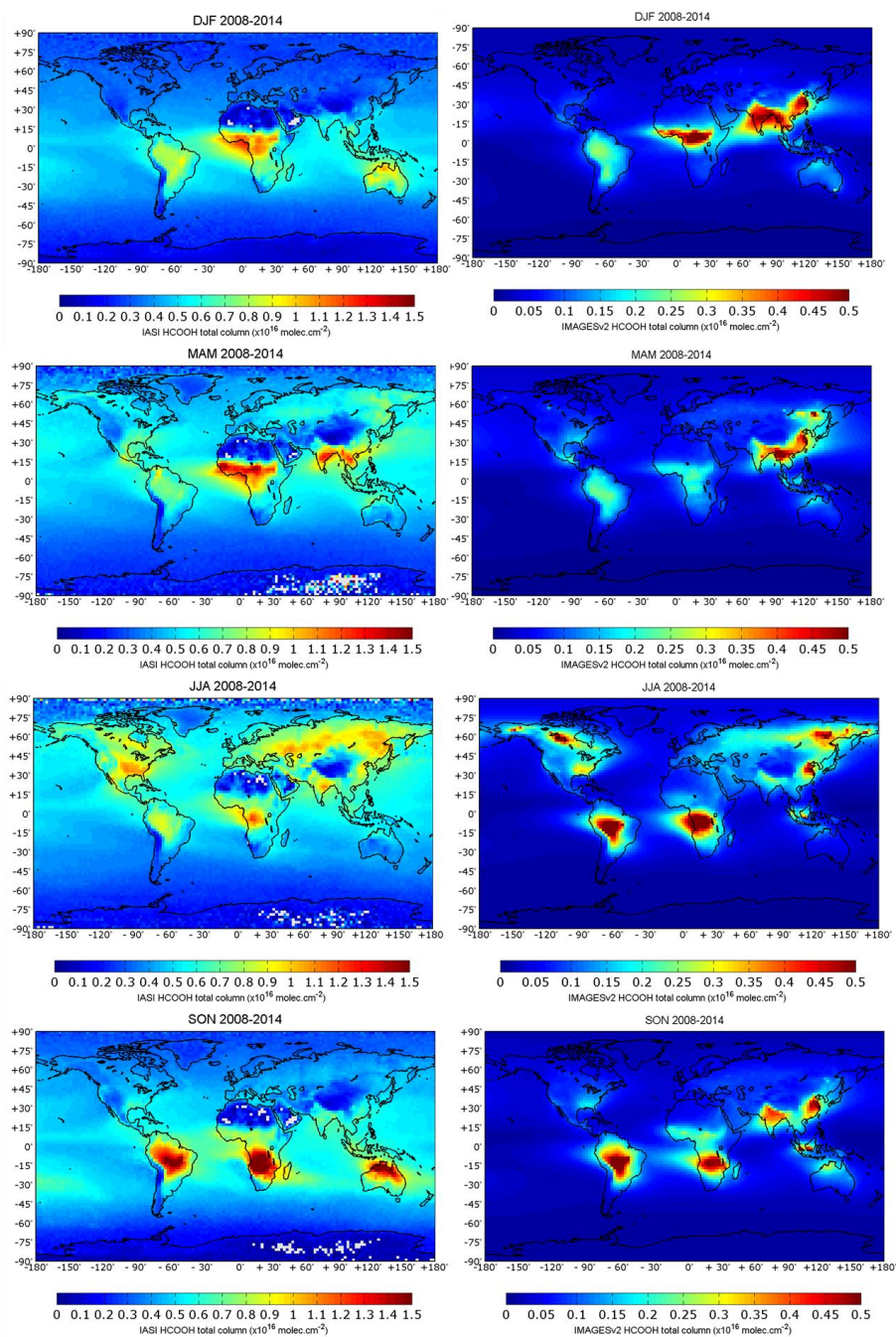


Figure 11. Seasonal HCOOH global distribution from 2008 to 2014 derived using the IASI radiance observations, gridded to IMAGESv2 horizontal resolution (2° lat \times 2.5° lon) (left panel), and from IMAGESv2 (right panel). DJF=December-January-February, MAM=March-April-May, JJA=June-July-August, SON=September-October-November. Note the different color scale between both distributions.

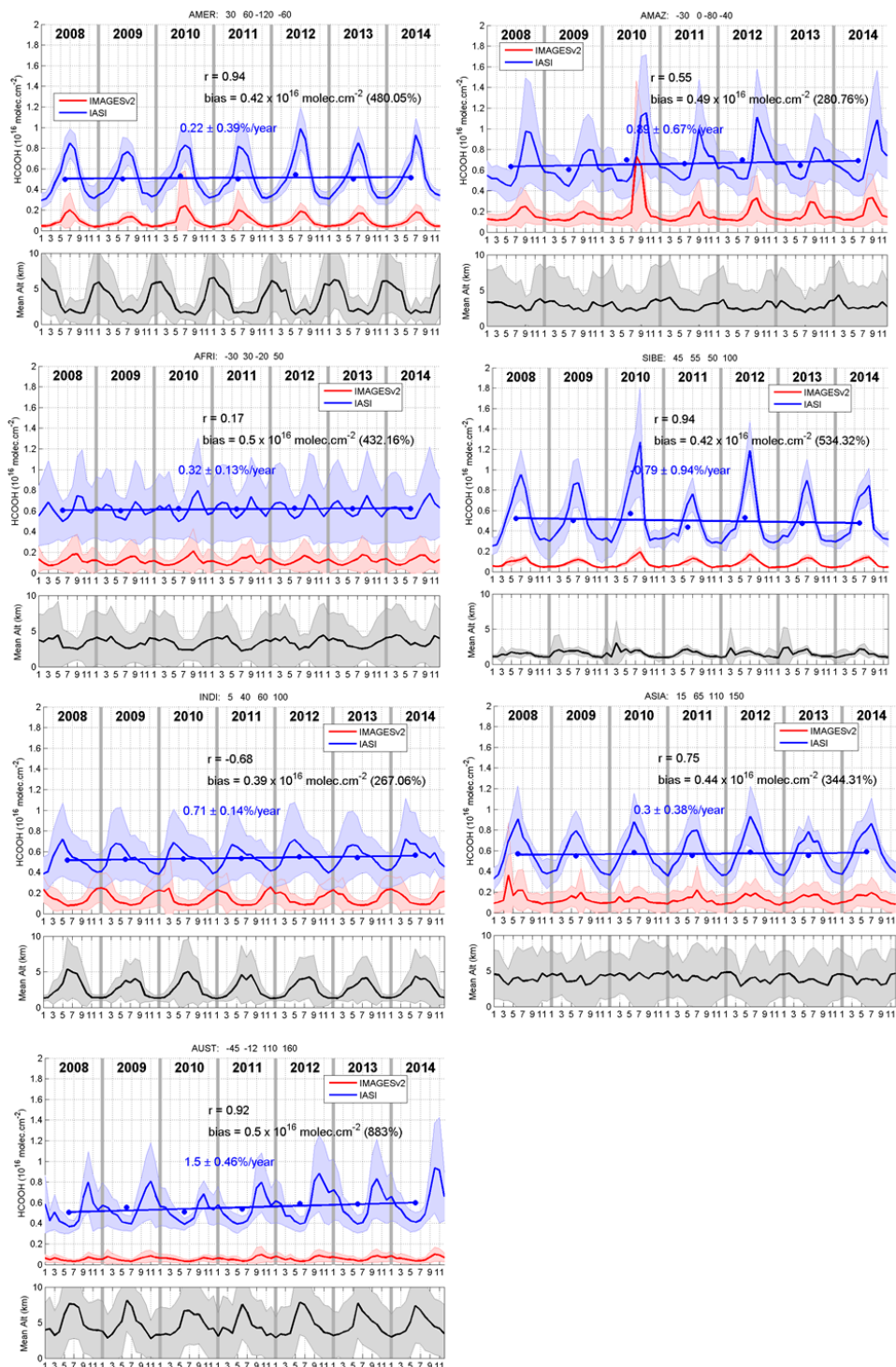


Figure 12. Time-series of the monthly HCOOH column means for IASI (blue) and IMAGESv2 (red) over different regions highlighted by black boxes in Fig. 1, between 2008 and 2014. The coordinates of each box (latitude and longitude) are written on the top of each plot. The red and blue shaded areas correspond to the monthly standard deviation. The correlation coefficient, the mean bias and the normalized mean bias (in parentheses) for the full period are given on each plot. The blue dots correspond to the annual IASI mean. The linear regression on the annual IASI mean and the calculated linear trend are



also provided. On the bottom panel, the mean altitude of the maximum in the HCOOH vertical distribution from IMAGESv2 is plotted in black with the corresponding standard deviation represented by the black shade areas.